Article

Wind dispersal of battery-free wireless devices

https://doi.org/10.1038/s41586-021-04363-9

Received: 9 December 2020

Accepted: 16 December 2021

Published online: 16 March 2022

Check for updates

Vikram Iyer[1]✉, Hans Gaensbauer[2], Thomas L. Daniel[3] & Shyamnath Gollakota[1,2]✉

Plants cover a large fraction of the Earth's land mass despite most species having limited to no mobility. To transport their propagules, many plants have evolved mechanisms to disperse their seeds using the wind[1–4]. A dandelion seed, for example, has a bristly filament structure that decreases its terminal velocity and helps orient the seed as it wafts to the ground[5]. Inspired by this, we demonstrate wind dispersal of battery-free wireless sensing devices. Our millimetre-scale devices weigh 30 milligrams and are designed on a flexible substrate using programmable, off-the-shelf parts to enable scalability and flexibility for various sensing and computing applications. The system is powered using lightweight solar cells and an energy harvesting circuit that is robust to low and variable light conditions, and has a backscatter communication link that enables data transmission. To achieve the wide-area dispersal and upright landing that is necessary for solar power harvesting, we developed dandelion-inspired, thin-film porous structures that achieve a terminal velocity of 0.87 ± 0.02 metres per second and aerodynamic stability with a probability of upright landing of over 95%. Our results in outdoor environments demonstrate that these devices can travel 50–100 metres in gentle to moderate breeze. Finally, in natural systems, variance in individual seed morphology causes some seeds to fall closer and others to travel farther. We adopt a similar approach and show how we can modulate the porosity and diameter of the structures to achieve dispersal variation across devices.

Plants have evolved various mechanisms to use wind for seed dispersal over a wide area[1–4] including creating lightweight diaspores with plumose or comose structures that act as drag-enhancing parachutes[6,7]. Asteraceae plants, such as the common dandelion, produce plumed seeds containing a pappus, which is a bundle of bristly filaments[1]. The pappus increases the drag experienced by the diaspores, decreasing their terminal velocity. This helps prolong their descent and allows greater opportunity for lateral wind currents to disperse them outward from their release point. Empirical studies have shown that dispersal distance is inversely proportional to terminal velocity[8]; in dry, windy and warm conditions, dandelion seeds can travel as far as one kilometre[1,3]. The bristly filament structures also enable the ability to flip in mid-air to achieve a stable descent in a defined, upright orientation[5]. Successful seed dispersal also requires prevention of clustering so that not all seeds land in the same area. Although fluctuation in wind patterns allows for some level of dispersal variation, the unique morphology of individual seeds provides an additional factor that varies the travel distance[6,9].

These properties are highly attractive for the deployment of sensor networks that have a similar goal: disperse large numbers of low-cost sensors over a broad geographic area to enable wide-area sensing. Prior attempts of automated sensor network dispersal, however, have orders of magnitude larger and heavier aerodynamic structures[10,11] or use batteries for power[10–12].

Here we investigate designs inspired by plumed seeds to develop battery-free wireless devices that disperse in the wind. Many wind-dispersed seeds with plume structures seen in nature have evolved to be small and lightweight, as these are more efficient for producing drag with small payloads than are winged seeds[7]. For example, a dandelion seed measures roughly 14 mm and weighs around 1 mg (ref. [1]). Because terminal velocity scales with mass, the combination of milligram-scale weights and high drag coefficient makes long-distance wind dispersal a viable strategy. However, emulating this behaviour with wireless battery-free sensors poses four key challenges. First, this requires designing and fabricating a lightweight drag-enhancing structure similar to the pappus of a dandelion seed. Second, this requires considerable miniaturization of all the electronic components, including a computing platform, wireless communication module, sensor and power circuits. Third, although solar power harvesting eliminates the need for batteries, it introduces the challenge of limited and intermittent energy availability. Solar power harvesting also requires the cells to face the Sun. This precludes the use of traditional parachutes that could fold or get tangled and occlude the solar cells, and adds aerodynamic stability requirements to the drag structure so it can passively reorient itself and land upright. Fourth, to prevent clustering of the sensors after landing, we need to introduce varied morphology into individual sensors to ensure their widespread dispersion across the target area. In this article, we address extreme size, weight and power (SWaP) challenges outlined above and demonstrate wind dispersal of battery-free wireless sensors (Fig. 1a–e, Supplementary Video 1).

[1]Paul G. Allen School of Computer Science and Engineering, University of Washington, Seattle, WA, USA. [2]Department of Electrical and Computer Engineering, University of Washington, Seattle, WA, USA. [3]Department of Biology, University of Washington, Seattle, WA, USA. ✉e-mail: vsiyer@cs.washington.edu; gshyam@cs.washington.edu

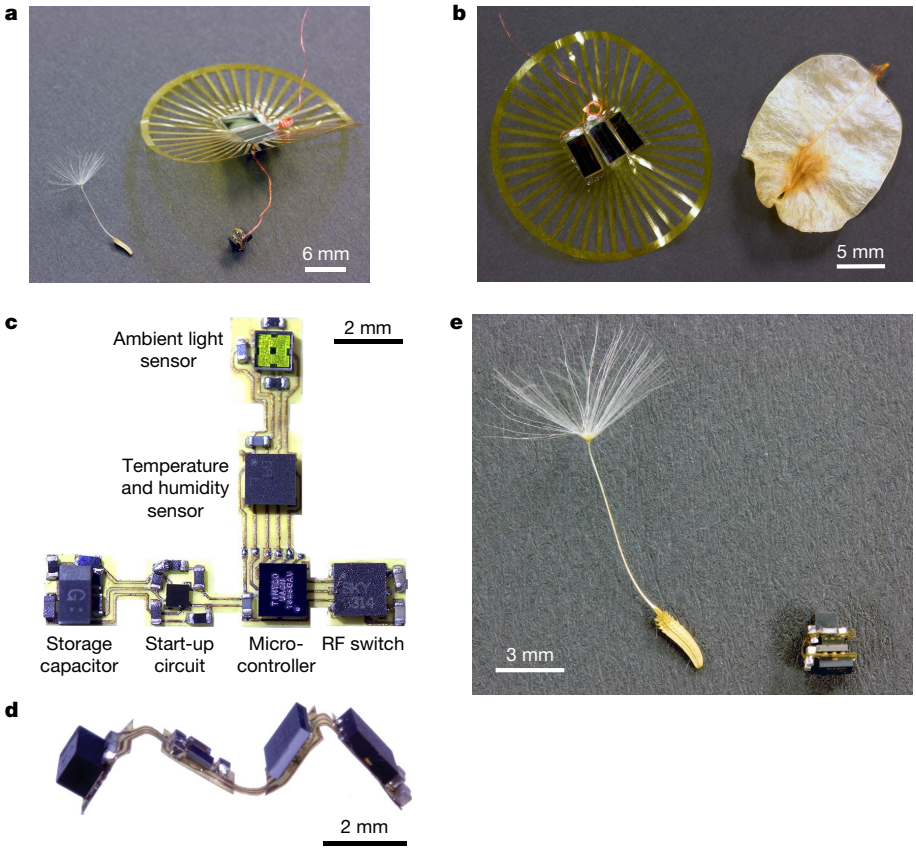

Fig. 1 | Wind-dispersed battery-free wireless devices. a, Battery-free wireless sensing device shown next to a dandelion seed. **b**, Top view of our battery-free wireless sensing device, showing its solar cells and drag enhancing structure next to an elm seed. **c**, Circuit showing the electronic components including sensors that can be attached. **d**, The circuit is made on a flexible substrate that can be folded. **e**, Circuit folded into a cube placed next to a dandelion seed.

Wind-dispersal mechanism

We have three goals: 1) develop a strategy to fabricate synthetic structures inspired by plumed seeds and investigate their payload capacity, 2) explore design strategies to introduce varied sizes and shapes into individual devices so they disperse to different distances, 3) determine the factors that affect aerodynamic stability to maximize the probability that the sensors descend in the correct upright orientation to harvest solar power after impact.

Plumed seeds such as dandelions consist of a porous disc made of a bundle of bristles extending from a central point. These structures produce a stable vortex of air above them[1] which increases drag compared to a solid disc and uses less material than a traditional parachute. Although exactly mimicking the three-dimensional (3D) bristles is challenging, terminal velocity scales with the projected area: $v(t) = \sqrt{2mg/(\rho A C_D)}$, where m and A are the mass and cross-sectional area of the device, g is the gravitational acceleration constant, and C_D and ρ are, respectively, the drag coefficient and fluid density. We approximate plumes with two-dimensional projections cut from thin polyimide films (7.5–25 µm) as shown in Fig. 1a, b and Extended Data Fig. 1 (see Methods for details). This material is commonly used for flexible circuit boards and enables us to produce varied shapes and scale the process for mass production. We augment the basic bristle structure with an outer ring to increase stiffness and minimize terminal velocity for larger payloads (see Supplementary Video 2 and Methods).

We systematically measure the terminal velocity for 75 designs (three materials of 7.5–25.4 µm, five diameters of 10–50 mm and five payloads of 20–70 mg) when dropped from 2 m. We perform empirical measurements owing to the complexities of accurately modelling the fluid–structure interactions for thin, deformable, freely falling objects. We calculate $C_D = mg/(\frac{1}{2}\rho v^2 A)$, which gives a measure of how efficiently the structure produces drag. We also calculate the Reynolds number, $\mathrm{Re} = \rho v d/\mu$, the ratio of inertial to viscous forces. Our results show that C_D increases as the Reynolds number decreases (see Fig. 2a); this follows a similar trend to natural plumed seeds[1,7] and all objects in flow (for example, spheres, cylinders)[13]. We note that the points with highest C_D are the smallest and lightest weight, which supports the advantages of miniaturization.

Figure 2b shows the relationship between terminal velocity and sensor weight for different film thicknesses. These data show first that increasing the diameter (and therefore the projected area A) results in lower terminal velocity, as expected; however, increasing to dimensions beyond 30 mm yields diminishing returns. Second, achieving terminal velocities below 1 m s^{-1}—where even light air flow to a moderate breeze (1–5 m s^{-1}) can result in wind dispersal greater than the release height—constrains sensor payloads to less than 70 mg. Third, Fig. 2a, b indicates, counter-intuitively, that greater film thicknesses (higher mass structures) generally perform better. A high-speed video of a 50-mm, 7.5-µm-thick disc carrying a 70-mg payload shows it deforming considerably as it falls (Supplementary Video 3). The edges bend inward owing to the low stiffness of the thin film, and so increased diameter beyond a point does not increase the projected area and is why thicker films perform better.

We emulate variation in seed morphology to attain further control over terminal velocity. In addition to bristles extending outward from the centre, species such as *Tragopogon pratensis* have orthogonal fibres[7]. We take inspiration from these to produce mesh patterns shown in Fig. 2c and Extended Data Fig. 2.

We empirically measure the terminal velocity of each design shown in Fig. 2c and plot the results versus the infill in Fig. 2d. The results follow

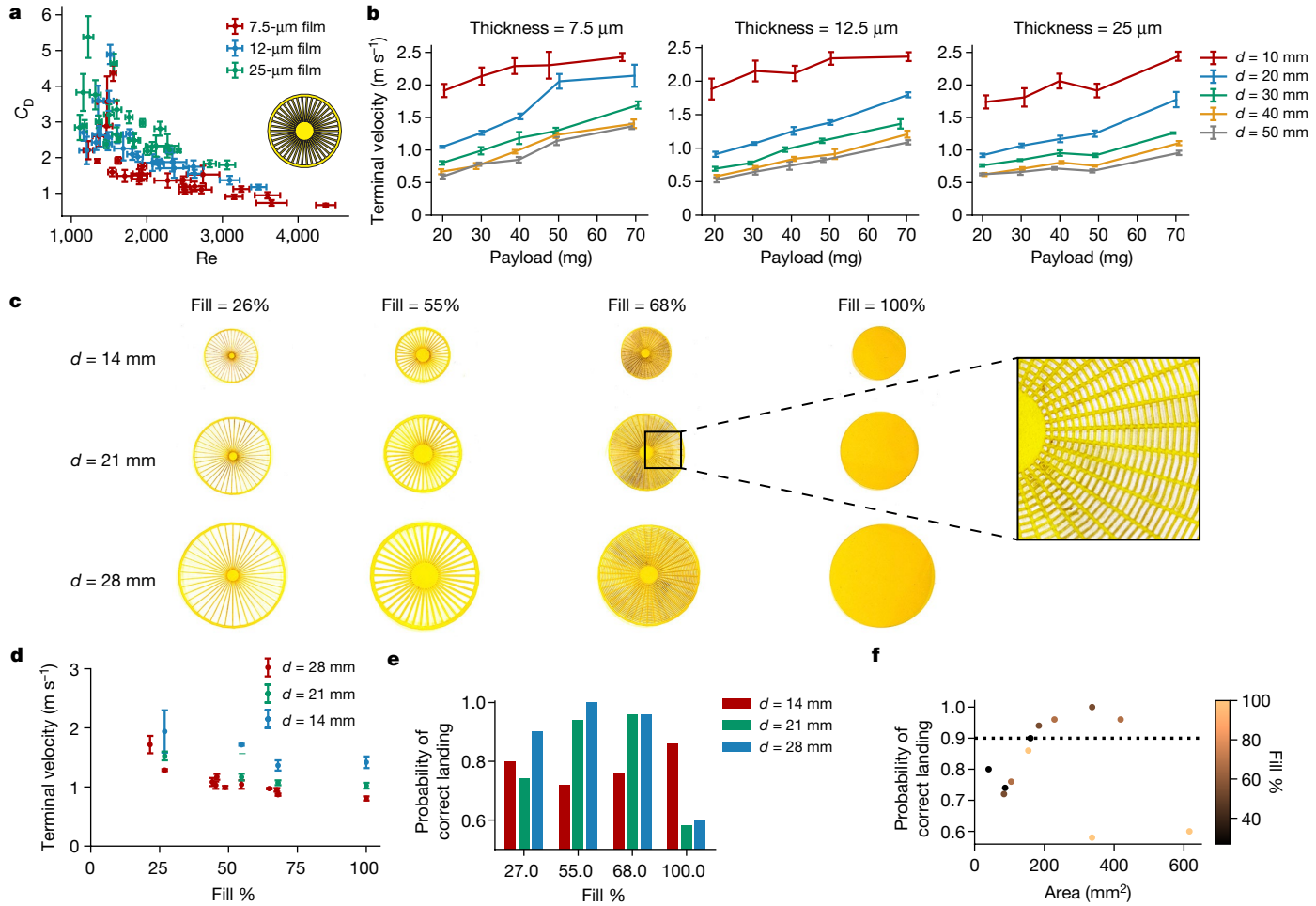

Fig. 2 | Wind-dispersal mechanism. a, Drag coefficient (C_D) versus Reynolds number (Re) for 75 designs (three film thicknesses, five diameters and five payloads, $N = 5$ trials per design, error bars = $\pm\sigma$). **b**, Terminal velocity versus payload for the same data shown in **a** ($N = 5$ trials per design, error bars = $\pm\sigma$). **c**, Designs of different sizes and fill patterns. **d**, Terminal velocity for designs from **c** on 12-μm films ($N \geq 3$ trials per design, error bars are $\pm\sigma$). **e**, **f**, Probability of upright landing versus fill percentage (**e**) and projected area (**f**; $N = 50$ trials per design).

the expected trend showing terminal velocity decreases as diameter increases. Increasing the filled area also decreases terminal velocity but with diminishing returns beyond 50% fill. The lowest terminal velocity, 0.81 ± 0.04 m s^{-1}, was achieved with a 28-mm-diameter disc and 100% fill. At 68% fill, the terminal velocities were 1.07 ± 0.04 m s^{-1} and 0.87 ± 0.02 m s^{-1} with 21-mm and 28-mm disc diameters, respectively. At disc diameters (14 mm) and fill fractions (10–25%) similar to a dandelion seed, the structure has a terminal velocity of 1.9 ± 0.36 m s^{-1} compared to the 0.39 m s^{-1} achieved by dandelion seeds, owing to the weight of our payload.

Although 100% infill results in the lowest velocity, similar to elm seeds (Fig. 1a), a solid disc has an unstable descent and tends to flutter and rotate as it falls, (Supplementary Video 4). By contrast, dandelion seeds maintain a stable descent and so we trade off a small decrease in terminal velocity for the porous structure with a stable descent. By placing the wireless device at the centre and adding curvature (see Methods and Extended Data Fig. 3), we can emulate the stable structure of a badminton shuttlecock. Stable descent in the correct orientation allows the sensors to harvest power and operate in mid-air.

Adding curvature causes the structure to right itself when dropped upside down (Supplementary Video 5). We measured the probability of upright landing by dropping each design with a 30-mg payload from a height of 2 m ($N = 50$ trials). At disc diameters equal to or greater than 21 mm, 100% infill causes instability and has an average 50% probability of upright landing, whereas a 26–68% infill results in a 90–100% probability (Fig. 2e). At a 14-mm diameter, the structure maintains a stable descent but does not always land in a consistent orientation. These results reveal a pattern: structures with an area below 160 mm^2, regardless of their diameter and infill patterns, are not large enough to produce the righting behaviour (Fig. 2f). Structures above this minimum area, and without a very high infill percentage, are stable and likely to land upright.

Battery-free programmable wireless sensors

The results above highlight the need for miniaturized sensing electronics. The conventional solution to this is to develop custom integrated circuits, as used in, for example, neural dust[14,15] and Michigan Micro Motes[16–18]. However, single monolithic integrated circuit solutions are often highly task specific. Moreover, prior works have not demonstrated fully functional battery-free sensors capable of passive wind dispersal at small (milligram) scales and have been limited to short communication ranges.

Our approach instead uses microcontrollers, which are small, general-purpose computing platforms that can interface with various sensors. Additionally, this method creates a highly accessible platform for researchers with diverse backgrounds to build on and rapidly prototype new applications at millimetre-scale without the considerable time, expense and expertise required to design custom silicon. We designed millimetre-scale, battery-free computing devices that weigh only 28.4 mg, and are fully integrated with backscatter communication

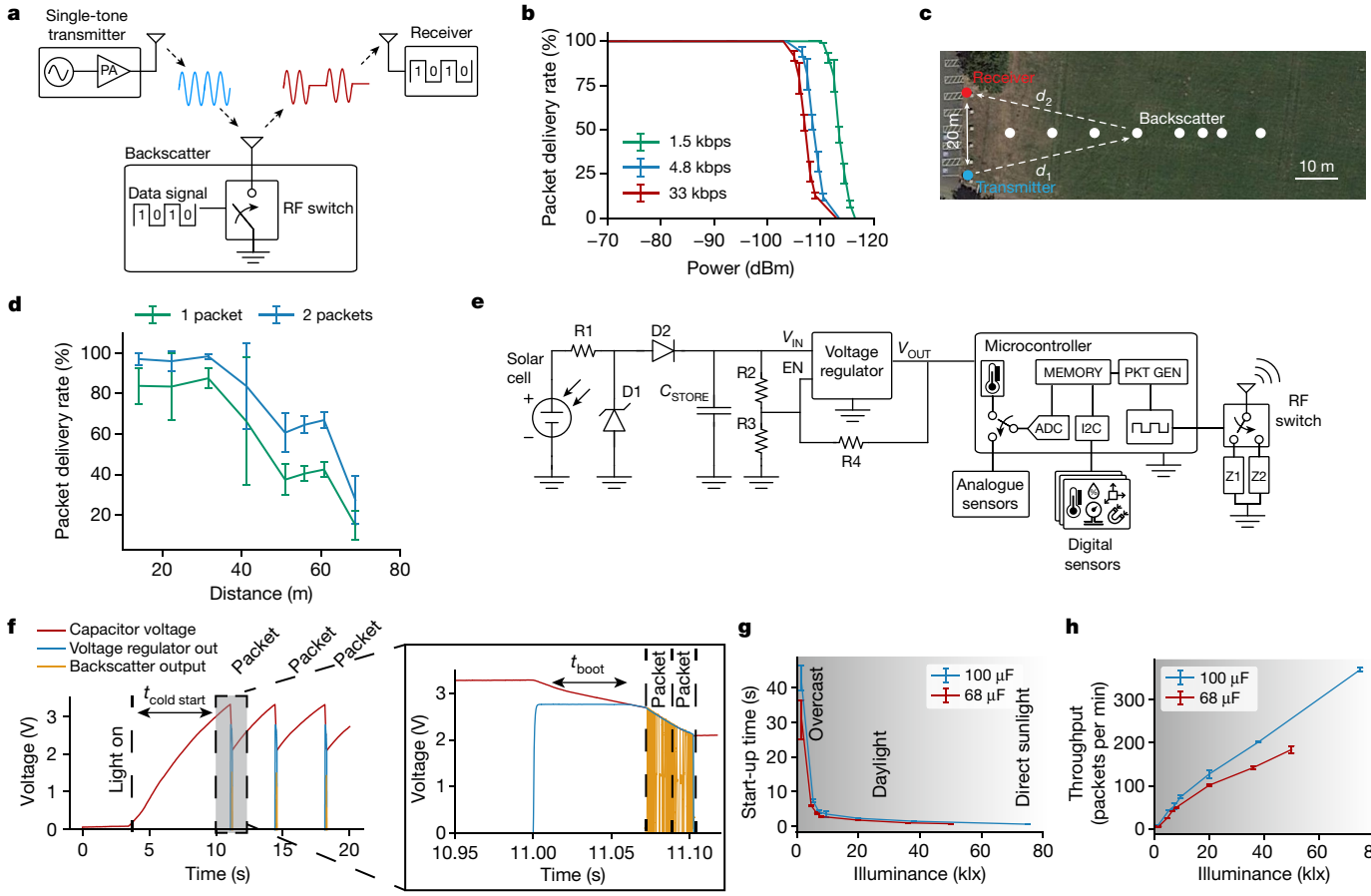

Fig. 3 | Battery-free wireless sensor. a, Backscatter system: a transmitter broadcasts a single-frequency tone, the backscatter device toggles an RF switch connected to an antenna, and a receiver decodes the backscattered data. PA, power amplifier. **b**, Error rate of backscattered packets received on an SX1276 radio at different power levels and bit rates in benchtop experiments ($N = 500$ packets per point, error bars = $\pm\sigma$). **c**, Set-up to test wireless range outdoors. The transmitter and receiver are placed 20 m apart and the backscatter device is moved away equidistant from both. Imagery from Google, ©2021 Maxar Technologies, US Geological Survey. **d**, In-air packet delivery rate measured outdoors versus range at 4.8 kbps with a single transmissions and 1× retransmission ($N \geq 100$ packets per point, error bars = $\pm\sigma$). **e**, Circuit block diagram. EN, enable; ADC, analogue-to-digital converter; PKT GEN, packet generation; R1–R4, resistor 1–resistor 4; D1–D2, diode 1–diode 2; Z1–Z2, impedance 1–impedance 2; I2C, Inter-Integrated Circuit; C_{STORE}, capacitor used for energy storage; V_{IN}, input voltage; V_{OUT}, output of voltage regulator. **f**, Wake-up sequence in continuous operation mode. Inset, magnification of the region around 11.00 s. t_{boot}, time to boot; $t_{cold\ start}$, cold-start time. **g**, **h**, Start-up time (**g**) and throughput (**h**) in continuous mode under outdoor light conditions, $N \geq 3$, error bars = $\pm\sigma$. klx, kilolux.

and power electronics (Fig. 1a, b). Each subsystem fits within about 2 mm × 2 mm with flexible interconnects to the next block, allowing the folded circuit to fit within a 3 mm cube (Fig. 1d, e). This dense packaging emulates the structure of many wind-dispersed seeds.

Our system is designed around the ATtiny20 microcontroller, which measures 1.56 mm × 1.4 mm and weighs 2.2 mg. However, the microcontroller lacks a radio for wireless communication or the circuits to power it. Our recent works on battery-powered millimetre-scale wireless sensors[12,19] use small Bluetooth radios for communication; these require external components such as crystal oscillators and weigh 166–248 mg. We instead designed a backscatter communication system that allows communication from the microcontroller, without a radio. A backscatter device operates by modulating its antenna impedance[20]. This produces a mixing operation at the antenna: an incoming radio signal is multiplied with the switch modulation signal (Fig. 3a). Backscatter decouples the energy- and size-expensive parts of a radio onto an external device that broadcasts a signal that the small, low-power sensor can reflect to communicate.

Range however presents challenges for backscatter. A radio transmission from a distance d incurs a path loss proportional to $1/d^2$. Backscatter has two links: one from the transmitter to the backscatter device (d_1), and another from the backscatter device to the receiver (d_2), incurring a path loss proportional to $1/(d_1^2 d_2^2)$. Thus, prior millimetre-scale, programmable backscatter systems have a 1–2 m backscatter range[21]. To improve this range, we performed coding and modulation on the microcontroller to mimic signals expected by high-sensitivity commodity radio receivers (SX1276, Semtech) that can decode on–off keying signals down to −117 decibel-milliwatts (dBm). Our transmitter broadcasts a single tone (see Methods and Extended Data Fig. 9 for full duplex version), and the microcontroller backscatters a packet with the expected preamble, header and format (see Methods and Extended Data Fig. 4). Although prior work has shown long-range backscatter communication using chirp spread spectrum[22], these systems are heavy and perform more power and computationally intensive modulation. By contrast, our design runs on small form factor microcontrollers and meets our size, power and weight constraints.

The transmissions from our backscatter devices support multiple bit rates and can be successfully decoded at signal levels as low as −111 dBm (Fig. 3b). In an open field (Fig. 3c), 4.8-kilobits per second (kbps) backscatter transmissions were decoded with a packet delivery rate of 66–88% up to 41 m; this increased to 84–98% when each transmission was repeated twice (Fig. 3d). Packet repetition enables reliable reception in the absence of acknowledgements (see Methods for detailed discussion of scaling transmissions up for larger networks and see simulations in Extended Data Fig. 5).

Table 1 | Component weights

Subsystem	Component	Weight (mg)
Power	Solar cells	9
	Capacitor	6.3
	Start-up circuit	1.8
Computing	Microcontroller	2.2
Backscatter	RF switch	3.6
	Antenna	1.7
Miscellaneous	PCB + solder	3.8
	Glue/wires	2
Drag structure	*d* = 28 mm, 55% fill	6.6
Total		**37**

Weight breakdown of each of the components in the battery free wireless sensor. Note that the total weight may differ from the specific configuration shown depending on the choice of sensors and drag structure design.

Harvesting circuitry

Solar energy allows our sensors to operate battery-free for reduced weight and longer lifetime; however, the variability of sunlight poses challenges for robust operation. Considering the absence of sunlight overnight, the system must 'cold start' from a powered-off state. This is challenging because the microcontroller takes 4–5× more energy to boot up than to backscatter data. We include a capacitor that can accumulate solar energy sufficient for brief sensing and backscatter, but when starting up from a discharged state the capacitor does not have enough energy to buffer the start-up transient. If the solar cell output is insufficient, the microcontroller gets stuck in a loop of attempted starts.

To address this, we design a start-up circuit for near-zero-power monitoring of the capacitor voltage that triggers system start up. The circuit has a low dropout regulator with a voltage divider, consisting of two resistors, connected to the enable pin of the regulator (Fig. 3e). A third large resistor tying the enable to the output adds hysteresis after start up.

Table 2 | Sensors

Sensor	Sensor mass (mg)	Memory (B)	Mode	Power 1Hz (µW)	Power 0.1Hz (µW)
Light	1.4	608	Internal timer	111.4	22.7
Temperature / humidity	2.6	616	Internal timer	44.6	16.0
Temperature+ humidity	2.6	676	Internal timer	47.9	16.3
Light+ temperature+ humidity	4.0	780	Internal timer	135.6	25.1
Light+ temperature+ humidity+ pressure	12.4	922	Internal timer	254.4	37.0
Magnetometer	0.8	832	Internal timer	92.9	20.5
Temperature / humidity	2.6	674	External timer	20.9	2.8
Temperature+ humidity	2.6	734	External timer	24.0	3.2
Light+ temperature+ humidity	4.0	838	External timer	111.1	11.9

Sensor weight, memory requirements and power measurements in different operating modes.

Figure 3f shows the system starting from near 0 V and operating in a mode where it repeatedly backscatters sensor data. The red line shows the capacitor charging up. After it crosses the 3.3-V cold-start threshold (causing the enable voltage to exceed 0.7 V), the voltage regulator output (blue line) increases to 2.8 V. The microcontroller starts and backscatters a burst of packets. Upon reaching its negative threshold, the system turns off to avoid complete discharge. Figure 3g shows the time required to cold start under different outdoor lighting conditions down to 1,400 lx (see Extended Data Fig. 6 for indoor lighting results and power harvested outdoors). At 500 lx, the variance in start-up time increases to 8.01 min. Figure 3h shows the throughput in continuous sampling mode with two different storage capacitors. The weights of all components are shown in Table 1.

After start up, we can also leverage the sleep modes of the microcontroller to sample data at a consistent rate with minimal power. We demonstrate two sleep modes in Table 2 where the microcontroller performs duty-cycled operations and spends most of its time in a low-power mode with all of its peripherals OFF. Using either a low-frequency internal timer on the microcontroller, or even lower-power timers available on sensors, the system stays ON continuously, periodically waking up to sample and transmit data before returning to sleep (see Methods).

We demonstrate operation in sleep modes with sensors capable of measuring temperature, humidity, light, pressure, magnetic fields and acceleration. These sensors are chosen owing to their small size and weight, and low average power. Each communicates data using the Inter-Integrated Circuit (I^2C) protocol. We demonstrate operation at various sampling rates in the sleep modes described above for different sensors and combinations of sensors and show the results in Table 2 and Extended Data Table 1.

Outdoor and sensor evaluation

We performed experiments outdoors in varying wind conditions and heights up to 22 m (Supplementary Video 6, details in Methods and Extended Data Fig. 7). Higher drop heights allowed the sensor to be carried further by a wind gust during a longer descent and increases variance (Fig. 4a–c, see Methods for wind condition details). The point recorded at 100 m was dispersed by a strong wind gust indicated by the large variance in Fig. 4c. During the experiments, the wind blew in the same direction along which the sensors travelled. We also compared two designs in low wind to show how they can prevent clustering (Fig. 4d).

We also evaluate each of our sensors in real-world scenarios. Figure 4e–h shows operation of multiple environmental sensors outdoors for 4.5 h until sunset, and successful cold start after sunrise. A sensor fusion method to reduce error is discussed in Methods section 'Light-based temperature and humidity correction' and Extended Data Fig. 8. Figure 4h shows that air pressure measurements are highly correlated to a reference sensor with a fixed offset due to altitude differences.

Figure 4i shows the polarity change in a magnetometer signal when a compact SUV drives by at 16 km h^{-1} within 3 m. Larger trucks would produce a signal and could be detected at longer range, which opens potential uses for conservation scenarios that require detecting vehicles used for illegal logging or poaching. Figure 4j shows 1-Hz readings from an accelerometer hovering above a vertical wind tunnel compared to readings from a reference anemometer. The high correlation between the accelerometer readings and the wind speed demonstrate that this sensor could reveal which direction the device is moving, or be used to collect distributed information about wind direction within a column of air as the devices descend.

Concurrent work by Kim et al.[23] on wind-dispersed devices focuses on fabrication techniques for 3D structures and presents extensive aerodynamic modelling. It also demonstrates a proof-of-concept electronics package weighing 90–217.7 mg that outputs a single, time-integrated readout from an analogue light sensor that can be interrogated by a near-field communication reader placed within a few centimetres.

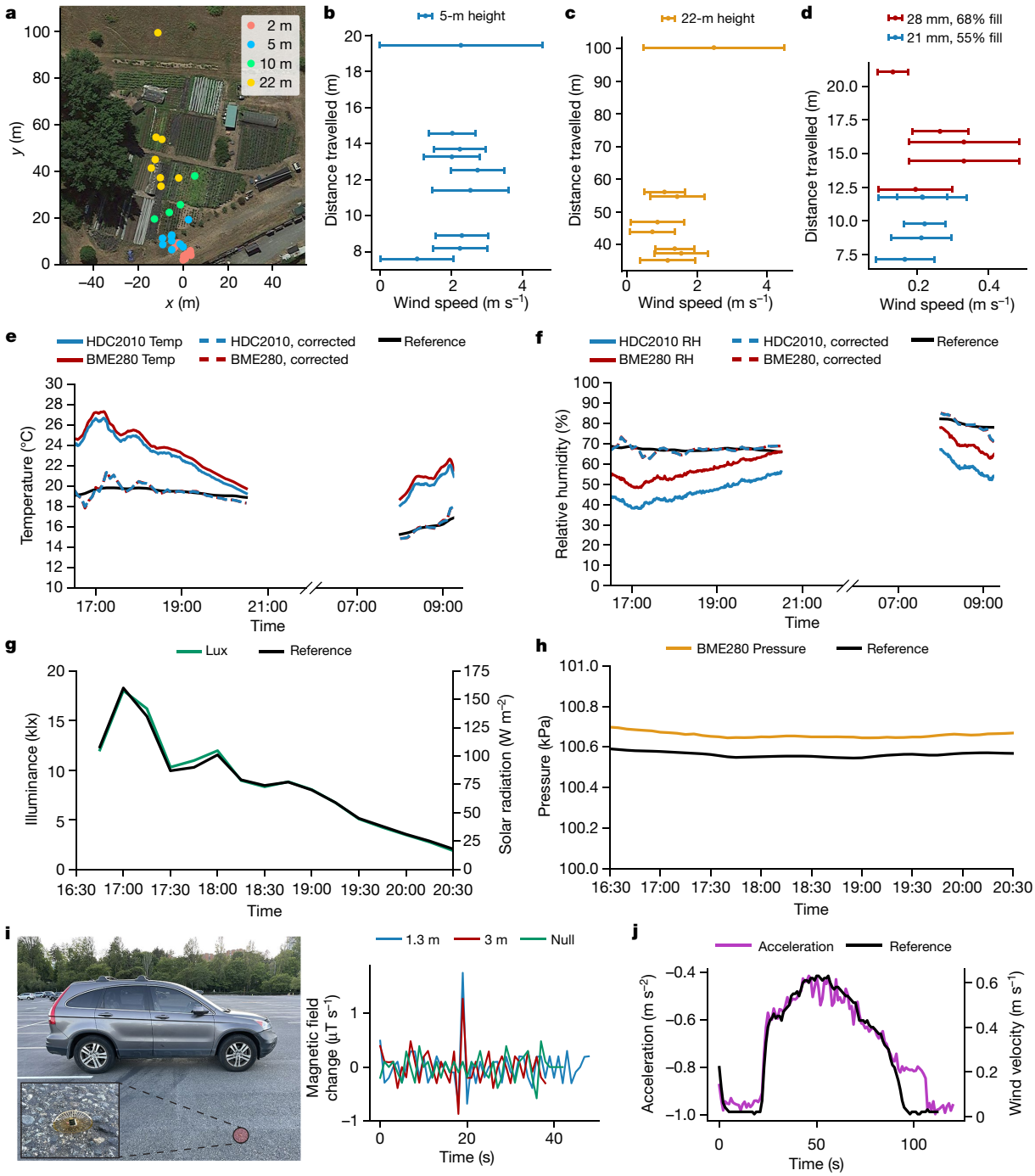

Fig. 4 | Outdoor evaluation. a, Landing locations in outdoor drop tests from increasing heights. Imagery from Google, ©2021 CNES/Airbus, Maxar Technologies, US Geological Survey. **b**, **c**, Wind speed versus distance for 5-m (**b**) and 22-m (**c**) drop heights (error bars = $\pm\sigma$, $N > 200$ wind speed values). **d**, Wind speed versus distance for two different structures (error bars = $\pm\sigma$, $N > 200$ wind speed values). **e**, **f**, Outdoor temperature (**e**) and relative humidity (**f**) measurements for two sensors over 6 h showing successful cold start and correction for Sun exposure using the onboard light sensor. **g**, Outdoor light sensor readings compared to reference solar radiation data. **h**, Outdoor pressure sensor data compared to a reference sensor. **i**, Magnetometer readings at 1 Hz from a passing car (right) and experimental set-up (left). **j**, Accelerometer readings at 1 Hz from a device in a vertical wind tunnel compared to anemometer readings.

By contrast, our work takes a systems approach that allows us to minimize the system weight, run an array of computing and sensing devices in low or variable light conditions as well as enable backscatter communication that can operate at distances of 60 m at a smaller size and form factor. This enables us to demonstrate a fully functional, wind-dispersed wireless sensing system and evaluate it in outdoor environments and real-world sensing applications.

Online content

Any methods, additional references, Nature Research reporting summaries, source data, extended data, supplementary information, acknowledgements, peer review information; details of author contributions and competing interests; and statements of data and code availability are available at https://doi.org/10.1038/s41586-021-04363-9.

1. Cummins, C. et al. A separated vortex ring underlies the flight of the dandelion. *Nature* **562**, 414–418 (2018).
2. Lentink, D., Dickson, W. B., van Leeuwen, J. L. & Dickinson, M. H. Leading-edge vortices elevate lift of autorotating plant seeds. *Science* **324**, 1438–1440 (2009).
3. Greene, D. F. The role of abscission in long-distance seed dispersal by the wind. *Ecology* **86**, 3105–3110 (2005).
4. Greene, D. F. & Johnson, E. A. The aerodynamics of plumed seeds. *Funct. Ecol.* **4**, 117–125 (1990).
5. Sheldon, J. C. & Burrows, F. M. The dispersal effectiveness of the achene–pappus units of selected Compositae in steady winds with convection. *New Phytol.* **72**, 665–675 (1973).
6. Andersen, M. C. Diaspore morphology and seed dispersal in several wind-dispersed Asteraceae. *Am. J. Bot.* **80**, 487–492 (1993).
7. Casseau, V., De Croon, G., Izzo, D. & Pandolfi, C. Morphologic and aerodynamic considerations regarding the plumed seeds of *Tragopogon pratensis* and their implications for seed dispersal. *PLoS ONE* **10**, e0125040 (2015).
8. Augspurger, C. K. & Franson, S. E. Wind dispersal of artificial fruits varying in mass, area, and morphology. *Ecology* **68**, 27–42 (1987).
9. Andersen, M. C. An analysis of variability in seed settling velocities of several wind-dispersed Asteraceae. *Am. J. Bot.* **79**, 1087–1091 (1992).
10. Edwards, D. J. et al. CICADA flying circuit board unmanned aerial vehicle. In *2018 AIAA Aerospace Sciences Meeting* 1008 (AIAA, 2018).
11. Pounds, P. & Singh, S. Samara: biologically inspired self-deploying sensor networks. *IEEE Potentials* **34**, 10–14 (2015).
12. Iyer, V., Kim, M., Xue, S., Wang, A. & Gollakota, S. Airdropping sensor networks from drones and insects. In *MobiCom '20: Proc. 26th Annu. Intl Conf. Mobile Computing and Networking* 61 (ACM, 2020).
13. Vogel, S. *Life in Moving Fluids: The Physical Biology of Flow* 2nd edn (Princeton Univ. Press, 2020).
14. Seo, D. et al. Wireless recording in the peripheral nervous system with ultrasonic neural dust. *Neuron* **91**, 529–539 (2016).
15. Kahn, J. M., Katz, R. H. & Pister, K. S. J. Next century challenges: mobile networking for "Smart Dust". In *MobiCom '99: Proc. 5th Annu. Intl Conf. Mobile Computing and Networking* (eds Kodesh, H. et al.) 271–278 (ACM, 1999).
16. Lee, Y. et al. A modular 1 mm^3 die-stacked sensing platform with low power I^2C inter-die communication and multi-modal energy harvesting. *IEEE J. Solid-State Circ.* **48**, 229–243 (2013).
17. Chen, Y. et al. Energy-autonomous wireless communication for millimeter scale Internet-of-Things sensor nodes. *IEEE J. Sel. Area Commun.* **34**, 3962–3977 (2016).
18. Chuo, L.-X. et al. A 915 MHz asymmetric radio using *Q*-enhanced amplifier for a fully integrated 3 × 3 × 3 mm^3 wireless sensor node with 20 m non-line-of-sight communication. In *IEEE Intl Solid-State Circuits Conf.* 132–133 (IEEE, 2017).
19. Iyer, V., Najafi, A., James, J., Fuller, S. & Gollakota, S. Wireless steerable vision for live insects and insect-scale robots. *Sci. Robotics* **5**, abb0839 (2020).
20. Rostami, M., Sundaresan, K., Chai, E., Rangarajan, S. & Ganesan, D. Redefining passive in backscattering with commodity devices. *MobiCom '20: Proc. 26th Annu. Intl Conf. Mobile Computing and Networking* 3 (ACM, 2020).
21. Iyer, V., Nandakumar, R., Wang, A., Fuller, S. B. & Gollakota, S. Living IoT: a flying wireless platform on live insects. In *MobiCom '19: 25th Annu. Intl Conf. Mobile Computing and Networking* (eds Agarwal, S. et al.) 5 (ACM, 2019).
22. Talla, V. et al. LoRa backscatter: enabling the vision of ubiquitous connectivity. In *Proc. ACM Interactive, Mobile, Wearable and Ubiquitous Technologies* 105 (ACM, 2017).
23. Kim, B. H. et al. Three-dimensional electronic microfliers inspired by wind-dispersed seeds. *Nature* **597**, 503–510 (2021).

Methods

Wind-dispersal structure

Successful wind dispersal requires a structure that produces drag and reduces the terminal velocity. Intuitively, the slower the seed falls, the greater chance it has for horizontal displacement by the wind. Two common drag-enhancing structures used by seeds are plumes, for example, dandelion seeds, and winged structures such as those seen in species of maple trees (for example, *Acer saccharinum*). Winged seeds autorotate to produce lift by generating a leading-edge vortex[25], whereas plumed seeds tend to operate at lower wing loading and benefit from a sharp increase in drag coefficient at low Reynolds number[7,8]. We explore the latter option as inspiration for miniaturized wireless sensing devices that operate in this regime, owing to its simplicity and scaling potential. We note that prior works have used different structures to disperse sensors; however, these are larger and heavier[10,11,24].

The structures were designed to minimize terminal velocity, to be aerodynamically stable, and to fall in a defined orientation so that the solar cell points upwards after impact. To do this, we designed various bio-inspired structures using laser micromachining methods. First, we wrote software to generate the desired patterns. These included simple designs consisting of thin rectangles rotated around a central point to model a two-dimensional projection of a dandelion seed pappus and designs for other features, such as the outer ring and the concentric circles to increase the filled area similar to the patterns seen in bird feathers. We then used a laser cutter to cut thin polyimide films (12 μm, Dupont Kapton) from these patterns. This produced flat, patterned structures. To give them a defined curvature and 3D structure needed to maintain a consistent orientation when they fall, we placed the patterned piece of polyimide in a curved mould; the mould consists of a 3D-printed plastic cube with a 7.7-cm-diameter cylinder cut out (Extended Data Fig. 3). We apply a small piece of double-sided tape to retain this shape and attach the solar cells. The electronics are attached on the opposite side. Although we produced the drag-enhancing structure and electronics separately, they could be integrated by patterning the traces onto a sheet of copper-coated polyimide.

To measure the terminal velocity for each structure, we dropped it with a 30-mg payload from a 2-m height (n = 20). The experiments were conducted indoors in a lab environment with minimal lateral airflow. To compute the probability of a design falling in the correct orientation, we again dropped each structure with a 30-mg payload. For each trial, the structure is held vertically with a pair of tweezers (thin side facing the ground) and released from the 2-m height. We note the landing orientation for each trial to determine the probability of correct landing (n = 50).

To perform the outdoor experiments, we selected a single structure (d = 28 mm, fill = 55%). We performed these experiments with a 30-mg weight attached at the centre, and we placed a hot wire anemometer (405i, Testo) at a height of 2 m, oriented in the direction with maximum wind speed. Experiments at each height were performed consecutively and during this time the wind blew in the same northerly direction. Wind speed recordings were started prior to the sensor release and stopped shortly after. Figure 4b, c shows the variance of the wind conditions along the direction travelled for the duration of the experiment. We note that the variance was calculated over at least 200 wind speed data points in each experiment where wind speed was sampled at 1 Hz. The exact length of experiments and therefore number of wind speed data points recorded varied depending on the wind speed and drop height. Our experiments were performed in temperatures ranging from 6 °C to 13 °C. Along the direction travelled by the sensors we observe an average wind speed of 1–2 m s^{-1} with occasional stronger gusts indicated by high variance.

For the 2-m height, structures were released by hand. For the 5-m height, structures were released from the top of a long pole. Distances to the landing locations when the devices were dropped from these heights are measured using a tape measure. Heights of 10 and 22 m were tested using a drone (Extended Data Fig. 7). A 51 AWG (American Wire Gauge) wire was attached to the structure and threaded through a hole on a printed circuit board attached to the drone. A loop at the end of the wire is threaded through the hole and hooked onto a solenoid, which is triggered remotely by a Bluetooth transmitter. When triggered, it retracts and releases the wire, allowing the device to fall. When the drone ascended to the target release height, a Bluetooth command was sent to trigger release. We observed that the airflow caused by the drone's propellers does not affect the motion of the device after it has descended more than 1 m. We then follow the sensors as they fall and record the final landing locations using GPS.

Tests with different designs were conducted using the drone from a 10-m height. We choose two designs different from the one tested previously. The first design has the same diameter but more fill (28 mm, 68% fill), and the second has the same fill as in previous trials but a smaller diameter (21 mm, 55% fill). On the day these experiments were conducted, the wind speed was very low for all experiments (0–0.5 m s^{-1}).

Millimetre-scale backscatter sensor

Backscatter systems communicate using reflected signals instead of actively generating radio frequency (RF) transmissions. This greatly reduces the power required to communicate, because generating high-frequency RF signals can be the most power-consuming part of a communication system. A backscatter device encodes data in reflected signals by modulating its radar cross-section using both the antenna and the components connected to it. An impedance boundary between two media allows a fraction of the signal to pass through it and the remainder to be reflected. By choosing two different impedances, we produce two different reflective states to communicate information. We therefore toggle between an open and a short circuit state. Although these two states should ideally produce a +1 and −1, respectively, components such as switches introduce losses; our implementation has a loss of −2.21 dB. We connect the output of the backscatter circuit to a lightweight antenna. To design an antenna of minimum size, we use a 70-mm-long piece of 43 AWG wire. To make it resonant at 915 MHz, we coil the wire for 12 turns with a 1.4-mm radius at the base. The resulting antenna has a −5 dB loss compared to a typical 915-MHz monopole antenna.

To achieve long-range transmissions, we repurposed a sensitive radio receiver (SX1276, Semtech). However, this chip requires specific fixed-packet structures that it is designed to decode. Although our goal is to control the backscatter signal and produce the appropriate packet structure, we are constrained by our small form factor microcontroller (ATtiny20, Atmel). Although the Semtech SX1276 receiver supports different modulations, such as chirp spread spectrum and frequency shift keying, the microcontroller limits us to operate using its on–off keying mode to send digital data. We ran the ATtiny microcontroller at 8 MHz, which constrains the bandwidth and resolution of the frequency shift keying signals it can produce. To generate on–off keying modulation a '1' bit is communicated by the presence of an RF signal, and a '0' bit by its absence. This can be implemented by toggling the microcontroller's output ON and OFF.

In addition to choosing a sensitive receiver, we must also reduce the interference it will receive directly from the Universal Software Radio Peripheral (USRP) transmitter broadcasting the RF carrier. To this end, we use a technique called subcarrier modulation, which sends data after applying an additional frequency shift. This technique adds some separation between the transmitter and the backscatter signal in the frequency domain, thus reducing interference. We leverage the fact that backscatter itself is a multiplication operation. So, to produce a frequency shift, we would ideally like to multiply the incoming signal with a sinusoid. Although an RF switch does not let us produce a sine wave, we can approximate this waveform using a square wave toggling between the two states at the same rate. If the square wave is

decomposed as a Fourier series, its primary component is a sine wave at the desired frequency, therefore producing the desired frequency shift. We choose a frequency offset of 4 MHz, which is determined by the maximum frequency of the microcontroller.

Extended Data Fig. 4 shows the packet structure the SX1276 is designed to receive. It consists of a preamble of at least 3 bytes that is a sequence of alternating ones and zeros (0xAA or 0x55). The receiver uses this structure to identify the start of a packet. The preamble is followed by a 4-byte address field that uniquely identifies a transmitter and an optional length field for variable packet lengths. The payload is followed by an optional 3-byte cyclic redundancy check (CRC).

To generate a packet, we first sample our sensor either using the microcontroller's analogue-to-digital converter (ADC) to read analogue sensors, or by sending a command using the I^2C protocol to read digital data from various external sensors described in further detail below. The data are sampled and stored in memory.

Next, the microcontroller constructs the packet which consists of fixed preamble bytes (0x555555), followed by a 4-byte address field and the sensor data payload as shown in Extended Data Fig. 4. We omit the CRC for 4.8 kbps and 1.5 kbps packets to reduce their length; however, this field may be used for higher bit rates (for example, 32 kbps). To generate an on–off keying signal with subcarrier modulation, a timer on the microcontroller is configured to output two complementary 50% duty cycle pulse-width-modulated (PWM) signals at the desired frequency. When these two outputs are enabled and connected to the switch, they produce a backscattered signal shifted by the subcarrier frequency. An assembly function translates the binary data to the appropriate delays to achieve the desired bit rate and toggles the PWM signal to produce the on–off keying modulation.

To measure the backscatter packet delivery rate in Fig. 3b, we use a bidirectional coupler to isolate the transmitter and receiver. A software radio (USRP E310) is configured to transmit a 919-MHz single tone into the input port of the bidirectional coupler, and the backscatter switch is connected to the output port. The receiver (SX1276) is connected at the output-coupled port through a series of attenuators, and the input-coupled port is terminated with a 50-Ω load. All devices are connected directly to the coupler's male-to-male SMA connectors and housed in metal containers to prevent weak radiated signals from propagating to the receiver. The microcontroller was programmed to send 100 packets with fixed data to measure the packet error rate. The signal's output power was varied by decreasing the USRP output. The power output of the packets was measured on a spectrum analyser (MDO4104-6, Tektronix). A total of 500 packets was sent for each power level, and these experiments were repeated for different bit rates. System performance is limited by the noise floor of the receiver, which increases with the bandwidth of the filter used at the receiver. The minimum filter bandwidth required to receive 33-kbps packets was 41.7 kHz. By contrast, 1.5-kbps packets could be received with a filter bandwidth of 12.5 kHz, resulting in a lower noise floor and improved sensitivity. Further decreasing filter bandwidth resulted in higher packet loss, probably owing to the frequency resolution of the microcontroller's oscillator.

For the range measurements outdoors, we set up the transmitter and receiver at one end of a field, 20 m apart. The receiver was the SX1276 module connected to an 8.5-dBi patch antenna (dBi, decibels relative to isotropic). A USRP was configured as a transmitter and connected to a power amplifier (RF5110G, Qorvo) to boost output power to 25 dBm. The transmitter is also connected to the same 8.5-dBi patch antenna. The antennas are both placed to radiate outwards onto the field. Owing to their radiation patterns, their parallel placement helps provide isolation. Packet error rates were collected by connecting the backscatter switch and microcontroller to our form factor wire antenna. The antenna consists of 12 turns of 43 AWG wire with a 1.4-mm diameter as well as a 17-mm-long straight length of wire as seen in Fig. 1a, b. It was held at a height of 1 m and moved to increasing distances away from the transmitter and receiver along a line perpendicular to their midpoint as shown in Fig. 3c.

Harvesting circuit

Small batteries either have very limited capacities[17] or add considerable weight to the payload[21]. We use thin film solar cells (40-µm thick, Microlink Devices) that provides up to 0.25 mW mm^{-2}. Using a solar cell still requires an energy storage element to operate in variable light conditions or in low light when the solar cell cannot provide enough power for continuous operation. We chose tantalum capacitors owing to their high energy density, which allows for a large capacitance in a small and lightweight package. The microcontroller requires 2.7 V or higher to run at the 8-MHz clock frequency used for subcarrier modulation described above; however, even in bright light conditions, a single 2.5 mm × 5 mm solar cell produces only 2.6 V. Instead of using a boost converter circuit, which could add substantial weight[19,26], we instead connect three small solar cell segments in series. We note that when operating in bright environments fewer cells could be used to reduce weight. Although this strategy of combining solar cells in series allows for consistent operation in low light conditions, it presents a problem for very bright light (for example, 1 sun); in bright sunlight the cells can produce a maximum voltage of over 7 V which is higher than the other circuit components can tolerate. To allow for robust operation across this spectrum of light conditions we add a 5.6 V Zener diode (D1) for protection at the input. At low voltage, current flow through the diode is 1 µA or less; however, when it approaches 5.6 V it allows excess current to flow to ground and prevents damage to the remainder of the circuit, such as the capacitor and voltage regulator, which are rated for a maximum of 6.3 V and 6.0 V, respectively.

Upon cold start, the chip waits for 64 ms to make sure the power supply is stable enough to power on the chip. This is followed by six additional oscillator cycles and 21 system clock cycles, during which configuration data are loaded before the system can begin executing programme instructions. To cold start, the capacitor must have buffered enough energy to begin executing instructions before it can enter its low-power modes for further operation. Our system therefore requires some method to sense charge level prior to being able to perform computation or logic. To do this with minimum power and size, we utilize the enable functionality of a 0.645 × 0.645 mm low-dropout voltage regulator (TCR3UG28ALF, Toshiba Semiconductor) to toggle the output on and off. We connect the input to the storage capacitor and the output to the microcontroller. To sense the charge level of the storage capacitor and trigger turning on the microcontroller, we use a voltage divider. By setting the ratio of the two resistors (7.6 MΩ and 3.49 MΩ), we can set the enable pin to exceed the required threshold to turn on (0.7 V) when the capacitor has reached a target voltage (3.3 V); however, this suffers the same problem as before: once the chip turns on and starts drawing power, capacitor voltage decreases and would cause the chip to turn off. To introduce the required hysteresis, we add an additional resistance (30 MΩ) to pull the enable pin up to the output. At start up, the output is floating, which has minimal effect. After the regulator turns ON, it uses this path to stay ON until encountering a negative threshold (2.1 V). This approach lets the microcontroller remain powered long enough to start up.

Power consumption and operating modes

After starting up, the system can operate in three modes.

a) Burst sampling. The CPU and all peripherals remain fully ON as long as power is available. This is most useful in scenarios with too little power to maintain the device in sleep. This mode allows the device to start up, transmit a few packets with its available energy, and turn off. The trade-off is long start-up times and lack of a programmable sampling rate. This mode also allows for maximum data rate outputs and could be used in scenarios with bright sunlight that allows for continuous operation. To operate in this mode, the chip is programmed to

execute instructions, for example, sampling sensors and transmitting data, in the main CPU loop that executes repeatedly.

b) Sleep with internal timer. The second operation mode utilizes the lowest-power sleep mode of the microcontroller, which powers down the main clock and all peripherals. We use the low-power watchdog timer to restart from this state without external hardware. This onboard timer runs at a low clock frequency and results in sleep power consumption of around 5 μA. The watchdog timer can be programmed to wake up periodically (for example, 0.125–60 Hz). In this mode upon start up all peripherals are turned off, and the chip is immediately set to go to sleep and wake up after the maximum 8-s delay to allow the capacitor voltage to recover from the high start-up power draw. Upon the first wake up from sleep, the device begins sampling and transmitting sensor data and the sampling rate can be increased. Each time the chip wakes up from sleep it samples sensor data and transmits it before returning to sleep. This mode requires harvesting enough energy to maintain the timer and make it through the first sleep cycle, but does not incur the cost of repeated start up and allows for a consistent sampling rate without the addition of other components.

c) Sleep with external timer. The chip can also be woken up from its lowest-power sleep mode by a signal sent from an external chip. The advantage of this is that it does not require running the onboard timer, and allows the use of even lower-power timing circuits integrated into many sensors. For example, the HDC2010 temperature and humidity sensor includes a programmable timer with a power consumption of <0.1 μA. This order-of-magnitude reduction allows for regular sampling rates at the lowest-power consumption as shown in Table 2. This also allows for even lower-power asynchronous, event-based sampling as the same temperature sensor, as well as other magnetometers, accelerometers and pressure sensors described also have onboard logic to trigger a wake-up signal only when the sensor data exceed a threshold. To enable this mode, upon start up, the chip immediately sends a command to the sensor to enable periodic wake up, and then proceeds to turn off all features and go into its lowest-power sleep mode. Upon receiving a wake-up signal, the device samples the sensor data and transmits it before returning to sleep.

We captured the waveform in Fig. 3f on an oscilloscope (MDO4104-6, Tektronix), starting with the system completely discharged. A desk lamp (OL-1, Phive) is turned ON at $t = 3.45$ s, and the red line indicating capacitor voltage begins to increase. Upon reaching a threshold, the voltage regulator turns on (blue line). The microcontroller enters its start-up phase (72 ms), after which it begins toggling the control signal to the RF switch to backscatter data (yellow line). We measured the time required for a cold start in Extended Data Fig. 6 and Fig. 3g under both indoor light conditions using LED lamps (LED-144, Amscope and LT-V9-15, GS Vitec) and outdoor natural light. Illuminance was measured using a lux meter (LX1330B, Dr. Meter) placed next to the solar cell. To determine cold-start time, we recorded the waveform on the oscilloscope and used it to measure the duration from when the circuit begins charging to when the microcontroller turns ON. We then measured the time between packets to determine throughput, shown in Fig. 3h. We performed these measurements for two different storage capacitors, 68 μF (AVX, F980G686MMA) and 100 μF (AVX, F980J107MMAAXE).

Sensor integration

We demonstrate operation of six different sensors on our platform capable of measuring temperature, humidity, light, pressure, magnetic fields and acceleration. These sensors are chosen owing to their small size and weight, and low average power. Additionally, certain sensors include low-power timing circuitry that can be used to wake up the microcontroller as described above. We demonstrate that each one is well within the limits of the computational capabilities of our microcontroller. Each of these sensors outputs digital data over an I^2C interface. Because this microcontroller does not have dedicated hardware to send I^2C commands as a primary device we implement this capability in software. Each time the microcontroller starts up or wakes up from sleep, it writes commands to the sensor to sample new data, waits briefly for the sampling to complete if necessary, and then reads the data into memory. The data are then transmitted via backscatter. We note that in the current implementation the data are read and transmitted as raw bytes and conversion to floating-point outputs and higher-level data processing is done at the access point to minimize the computation and power. Applications that require checking a threshold and other low-complexity operations can, however, be implemented onboard for specific applications.

Magnetometer-based car detection

To demonstrate a potential application of our wireless sensing device with an onboard magnetometer we demonstrate that it can detect a passing car. The magnetometer is placed on an asphalt surface in a parking lot as seen in Fig. 4i. The plot shows the pointwise difference between consecutive samples to highlight the change in polarity seen when a car or large metal object passes by. A compact SUV (Honda CR-V 2010) is driven past the sensor at a speed of 16 km h^{-1}. The magnetometer is sampled at a rate of 1 Hz. The experiment is repeated for two distances between the magnetometer and car (1.3 and 3 m). The plot also includes a null measurement for comparison when there was no car present.

Accelerometer-based wind measurement

A low power accelerometer (MC3672, MCube) is integrated with our 28-mm-wide 55% filled polyimide structure in Fig. 2c. The accelerometer consumes an average of 1.6 μA when set to sample in its ultralow-power mode at 50 Hz. The accelerometer is suspended in a vertical wind tunnel with an anemometer (405i, Testo) placed approximately 2 cm above it in the direction of air flow. The air-flow velocity of the wind tunnel is steadily increased and decreased while measured on both devices. Fig. 4j shows the x-axis measurement along with the anemometer measurements. We note that because the device was suspended, the z measurements remained roughly constant (acceleration due to gravity). The x and y measurements both show the same trend with small differences in magnitude and offset. Both the x and y measurements varied inversely (owing to the orientation of the accelerometer) with the flow velocity of the wind tunnel.

Network simulation

If a large number of our devices were to transmit simultaneously, their packets may collide and prevent the receiver from decoding them. We perform simulations based on measured data to explore three different strategies for scaling our design to larger networks. The first two leverage natural lighting variation, shown in Extended Data Fig. 5a, b and the third introduces a pseudorandom delay, shown in Extended Data Fig. 5c.

a) Natural lighting variation with no timer. In our outdoor tests of start-up time, variation in light conditions causes the devices to have different start-up times and charging rates that reduce the probability of collisions. Figure 3g and Extended Data Fig. 5a show the variance in start-up time for different light levels. The plots show that even under similar light conditions (trials for each light level were performed consecutively in the same location), small changes such as a passing cloud or shadow can affect the rate at which a device harvests power. In some cases, we observe a standard deviation of up to 0.8 s, which is orders of magnitude larger than the 13 ms required to send a 4.8-kbps packet. Extended Data Fig. 5b shows the start-up waveforms for two trials at around 9,650 lx, aligned to start at the same time. Different charging rates result in only one overlapping transmission period. Extended Data Fig. 5c shows a simulation with increasing network sizes. For each network size, 100 packet start times were generated for every node. Packet start times were sampled from a normal distribution (N) using

the mean (μ) and variance (σ^2) measured for each light level: $t_{start} \sim N(\mu_{lux}, \sigma^2_{lux})$, where ~ indicates 'distributed as'. Each of the 100 subsequent packet transmission times were also generated using the measured mean and variance for the inter-packet delay. Next, the packets for a randomly selected node were analysed to see whether other transmissions were within 1 packet length, indicating a collision. The count of collisions was used to compute its packet error rate. Packets are assumed to have 11 bytes (B) (7 B preamble + 4 B payload sufficient for two sensors) and transmitted at 32 kbps. This experiment was repeated 10 times to produce an average packet error rate experienced by a node in the network for a given network size. The results in Extended Data Fig. 5d indicate that for small networks with tens of nodes this may be a feasible strategy; however, network performance will vary during the day and it does not scale to large networks in bright light.

b) Start-up variation with fixed rate. The timer-based sleep modes on our device allow for transmitting packets at fixed intervals. A similar experiment described above was performed. Start-up times were generated based on the lowest lux level (1.4 klx) assuming all nodes in the network would be exposed to low light levels upon sunrise and continue from then on to operate in their fixed-rate mode. The inter-packet delay was set to fixed values available on the external timer. We assume here that compared to the packet lengths (milliseconds), variation in the sleep timers (with delays determined by >100-kHz clocks) would be negligible. The results in Extended Data Fig. 5e show, as expected, that high rates result in poor performance, but at rates below 1 packet per s, performance improves noticeably but with high variance.

c) Pseudo-random delay. To improve upon the fixed-rate method described above, we also explore a pseudo-random time offset, similar to Wi-Fi, as shown in Extended Data Fig. 5e. Instead of transmitting packets at a fixed interval of t_{fixed}, each device adds an additional pseudo-random time offset t_{random}; this can be easily generated on a microcontroller using a linear feedback shift register (LFSR) circuit. For each packet we set t_{random} to a randomly selected integer multiple of packet lengths up to a maximum of $8t_{packet}$. The results shown in Extended Data Fig. 5f show that this approach can support large networks where the data are transmitted at rates less than once every 10 s.

Light-based temperature and humidity correction

The weather station (Vantage Pro 2, Davis Instruments) shown in Extended Data Fig. 8a is designed to accurately measure air temperature and includes radiation shield and 24-h fan to cycle air through the enclosure. By contrast, our devices have minimal packaging aside from the thin polyimide film and solar cells and can therefore experience considerable heating when exposed to direct sunlight for extended periods of time. By integrating a light sensor, however, we can measure the effects of solar radiation and compensate for this effect. Fig. 4g shows the output of the onboard ambient light sensor averaged over 15-min intervals to match the sampling rate of the weather station's solar radiation sensor. This plot, as well as Extended Data Fig. 8b, shows that the two outputs are very highly correlated, showing that this sensor gives us accurate information about the amount of solar energy incident on the sensor. We next explore the relationship between the temperature error (difference between onboard sensor reading and the reference) and our light sensor output. Extended Data Fig. 8c, d shows that this relationship is also highly linear. To compensate for this effect we apply a linear regression over the temperature error for each sensor and illuminance data. Next we attempt to generate the error signal using the illuminance data and subtract it from the raw temperature readings to obtain the compensated output shown in Fig. 4e, f. The same method is used to correct the humidity data. We note that this simple linear correction method is a proof of concept demonstrating the advantage of including multiple sensors. This method could be further refined with additional data and more complex models considering our light sensor accurately captures the effects of solar radiation. Additionally, although this correction was done with comparison to a high-accuracy reference sensor that measures air temperature, future work could explore comparison to a reference sensor that measures ground temperature to build a measurement system for distributed ground-temperature measurements.

Improving communication and sensing capabilities

One of the limiting factors for range is the self-interference between the transmitter and the receiver. Using full-duplex radios that cancel the interference can help further increase the range as well as combine the transmitter and receiver into a single device. We prototype a system that can perform this cancellation in Extended Data Fig. 9a using a bidirectional coupler (ZGBDC6–362HP+, Minicircuits), phase shifter (RVPT0501GAC, RF Lambda), and variable attenuator (RVA-33, Minicircuits). Extended Data Fig. 9b shows the approximately 60 dB of cancellation achieved, which is in line with prior narrowband cancellation techniques[27]. Our small antenna has a 5-dB loss compared to typical 915-MHz monopole antenna; therefore, further optimizations could reduce the antenna loss and also increase the range. Communication range could also be improved by augmenting the sensor nodes to communicate with one another. Small, lightweight envelope detector circuits[21] can allow for a simple downlink to the microcontroller without adding a radio to the device to enable the devices to communicate. Devices could then relay messages, a particularly useful feature in a sensor network tasked with sensing a single event. For example, an abnormally high temperature indicating a fire could trigger a sensor to send an alarm signal that propagates through a network. Applications of this platform could further be augmented through integration with other sensing modules such as electrochemical gas sensors[28] and cameras. We note that recent miniaturized wireless camera systems[19] currently exceed our maximum payload of 70 mg; however, future work to improve the drag structure or reduce camera mass could enable this in the future.

Adding steerable descent and radio harvesting

One could consider better control of the placement of the nodes with steerable descent. This would require the addition of a lightweight, low-power actuator capable of modulating device shape. A shape-memory alloy or thin-film piezo material such as polyvinylidenefluoride (PVDF) are potential technologies that could be used to pull one side of the device inward to change its shape and trajectory, and our accelerometer could be used to give the system feedback. Shape changing could also be useful after landing to focus solar cells towards the Sun or aim a sensor in a specific direction. However, adding actuation is restricted by the amount of power available on the device, which highlights another limitation of the current work: it can operate only during the day. Allowing these devices to work at night requires either improved energy storage or an alternative harvesting method. The latter could be enabled using radio-power harvesting. For example, because the start-up circuit requires only a few microwatts of power to operate, a drone flying at a height of 15 m, transmitting at 36 dBm at 900 MHz would be sufficient to provide 10 μW of power at the device. Designing this system requires careful consideration of the frequency choice needed for powering versus backscatter communication to prevent interference and maximize the communication range.

Biodegradable structures and localization

The 3D structure accounts for the largest surface area and could be made of other materials, such as paper, that would biodegrade naturally. However, this still leaves unaddressed the problem of the small electronics themselves, which are not biodegradable. These electronics could be recollected by attaching a small magnet to the device for automated collection. We perform feasibility tests by attaching small N52 magnets to our device with a 30-mg payload (1 mm × 0.5 mm cylinder weighing 3 mg, 1 mm × 1 mm magnet weighing 23 mg). We observe that

they will attract and attach to a bar magnet within 3.5 cm and 4.5 cm, respectively. This opens the possibility of driving a vehicle with a large electromagnet across the deployment area to collect them. Collection times could be improved using backscatter localization capabilities to identify the approximate location of each sensor[29]. Another potential for lightweight localization is the addition of a non-linear diode to the device (3 mg), which has been used as part of harmonic radar for insect tracking[30].

Data availability

All data needed to evaluate the conclusions of the paper are available in the paper or in the Extended Data and Supplementary Information.

Code availability

Source code is available on a public GitHub repository for download: https://github.com/uw-x/wind_dispersal/.

24. Zussman, E., Yarin, A. & Weihs, D. A micro-aerodynamic decelerator based on permeable surfaces of nanofiber mats. *Exp. Fluids* **33**, 315–320 (2002).
25. Lentink, D., Dickson, W. B., van Leeuwen, J. L. & Dickinson, M. H. Leading-edge vortices elevate lift of autorotating plant seeds. *Science* **324**, 1438–1440 (2009).
26. James, J., Iyer, V., Chukewad, Y., Gollakota, S. & Fuller, S. B. Liftoff of a 190 mg laser-powered aerial vehicle: the lightest wireless robot to fly. In *2018 IEEE Intl Conf. Robotics and Automation (ICRA)* (ed. Lynch, K.) 3587–3594 (IEEE, 2018).
27. Katanbaf, M., Weinand, A. & Talla, V. Simplifying backscatter deployment: full-duplex LoRa backscatter. In *18th Symp. Networked Systems Design and Implementation* 955–972 (USENIX, 2021).
28. Shen, S. et al. An LC passive wireless gas sensor based on PANI/CNT composite. *Sensors* **18**, 3022 (2018).
29. Nandakumar, R., Iyer, V. & Gollakota, S. 3D Localization for Sub-Centimeter Sized Devices. In *SenSys '18: Proceedings of the 16th ACM Conference on Embedded Networked Sensor Systems* (eds Zhang, L. et al.) 108–119 (ACM 2018).
30. Riley, J. R. et al. Tracking bees with harmonic radar. *Nature* **379**, 29–30 (1996).

Acknowledgements We thank S. Kaplan and J. Smith for feedback on the manuscript and K. Johnson, V. Arroyos and B. Nguyen for help with experiments. This research is funded by Moore Inventor Fellow award #10617 and grant FA9550-14-1-0398 from the US Air Force Office of Scientific Research. S.G. is also funded by the National Science Foundation.

Author contributions V.I. designed and fabricated the hardware and performed experiments. S.G. and V.I. designed the overall system, experiments and evaluation. T.D. advised on the design and characterization of the drag-enhancing structures. H.G. implemented the backscatter code and sensor release mechanism used for outdoor testing. V.I. and S.G. wrote the manuscript; T.D. edited the manuscript. S.G. and V.I conceptualized the work.

Competing interests S.G. is a co-founder of Jeeva Wireless, Wavely Diagnostics, and Sound Life Sciences.

Additional information

Supplementary information The online version contains supplementary material available at https://doi.org/10.1038/s41586-021-04363-9.

Correspondence and requests for materials should be addressed to Vikram Iyer or Shyamnath Gollakota.

Peer review information *Nature* thanks Elizabeth Farrell Helbing and the other, anonymous, reviewer(s) for their contribution to the peer review of this work.

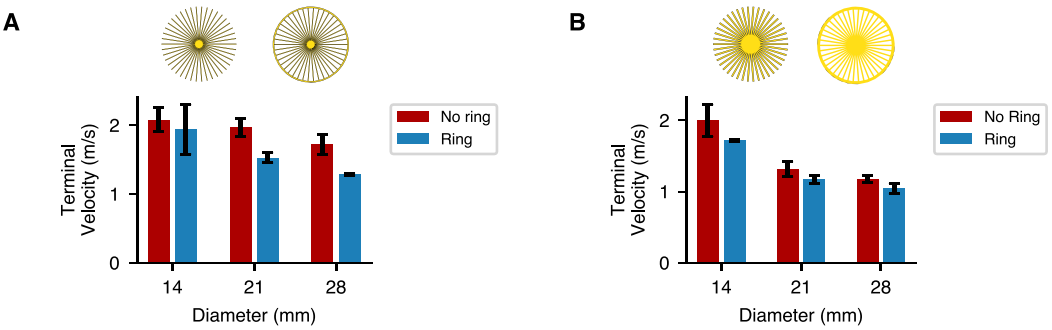

Extended Data Fig. 1 | Effect of outer ring on terminal velocity. a, Terminal velocities of 26% fill structures with different diameters using a 30-mg payload. **b**, Terminal velocities of 55% fill structures with different diameters with and without an outer ring using a 30-mg payload.

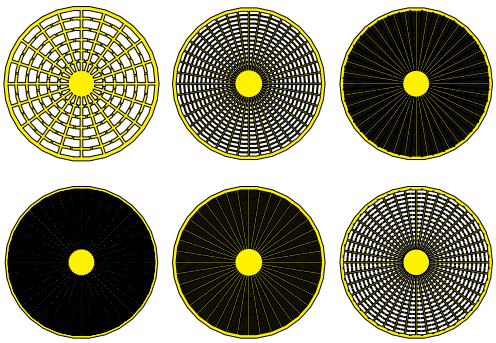

Extended Data Fig. 2 | Additional fill patterns. Additional fill patterns used to vary porosity. Changes include concentric circles connecting horizontal spokes extending out from the centre with various spacings, as well as additional cuts in the concentric circles between spokes.

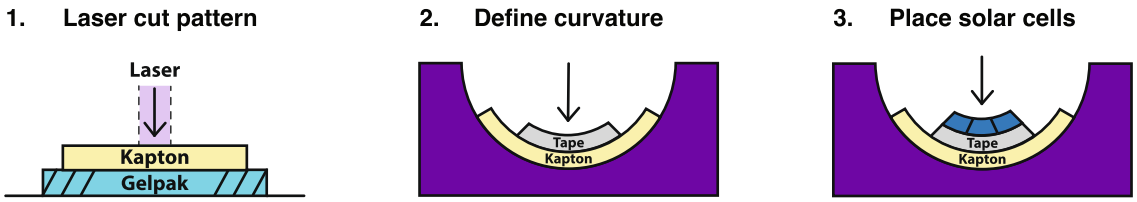

Extended Data Fig. 3 | Fabrication process. Fabrication process used to produce the curved drag enhancing structures.

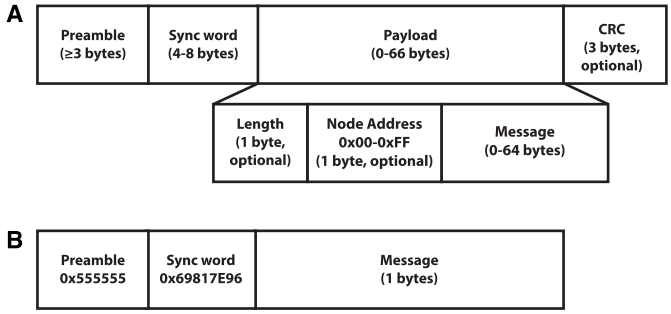

Extended Data Fig. 4 | SX1276 receiver on–off keying packet structure. **a**, Packet structure for the SX1276 receiver operating in on–off keying mode. **b**, Minimal packet structure used for testing the lower bit rates of 1.5 and 4.8 kbps. CRC, cyclic redundancy check.

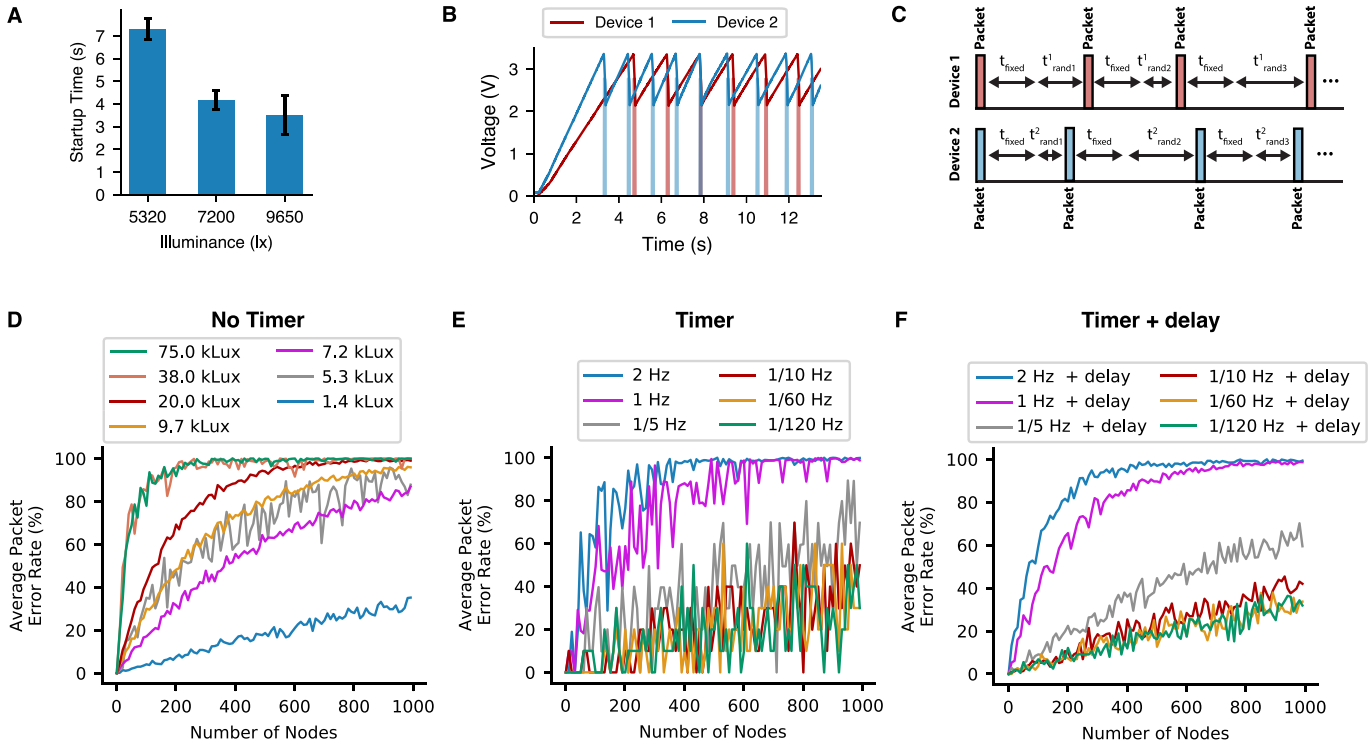

Extended Data Fig. 5 | Supporting transmissions from multiple devices. **a**, Natural variance of start-up time for outdoor measurements. **b**, Two waveforms recorded under similar light conditions show that natural variation in start-up time and time between packets reduces the probability of collisions. **c**, Addition of a random delay between each packet to reduce collisions. **d**, Network simulation of up to 1,000 nodes each transmit 100 packets. Node start and inter-packet transmission times are normally distributed based on power-harvesting data ($N = 100$ packets per node × 10 repetitions = 1,000). **e**, Network simulation with normally distributed start-up time assuming 1.4 klx followed by fixed 10-s delay between packets ($N = 1000$). **f**, Result of applying pseudorandom delays of up to 8 packet lengths with random start times assuming 1.4 klx ($N = 1{,}000$). The plot shows that this approach can support large networks where the data are transmitted at rates less than once every 10 s.

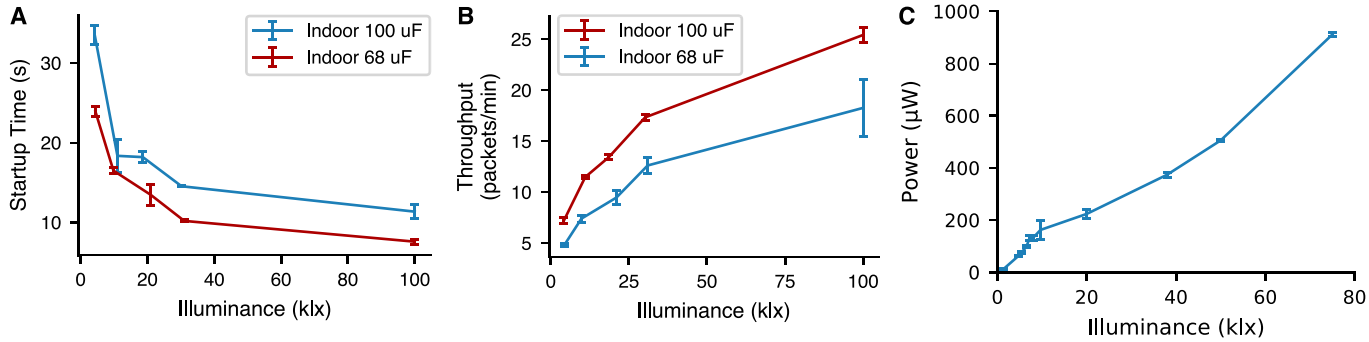

Extended Data Fig. 6 | Additional power harvesting results. a, Cold-start time required to charge the storage capacitor from zero to the time at which it can backscatter its first packet; measured using indoor LED lights ($N \geq 5$, error bars = $\pm\sigma$). **b**, Throughput of the sensor device after start up at different illumination levels indoors ($N \geq 5$, error bars = $\pm\sigma$). **c**, Measurements of power harvested at different light levels outdoors from our solar cells. ($N \geq 3$, error bars = $\pm\sigma$).

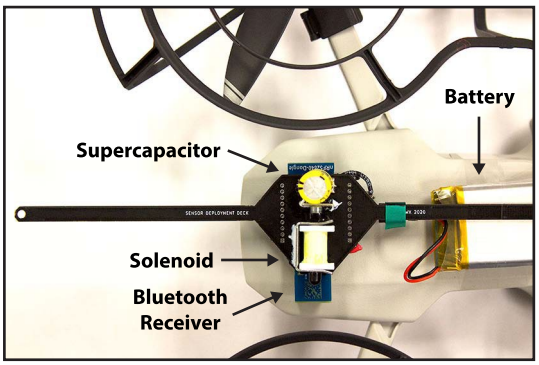

Extended Data Fig. 7 | Drone mechanism to drop the sensors. a, Small quadrotor with the mechanism used to drop devices from altitudes over 5 m outdoors. **b**, Drop mechanism consisting of a solenoid that can be wirelessly triggered by a Bluetooth transmission. Upon triggering, the supercapacitor keeps the solenoid retracted for a few seconds allowing the wire holding the sensor in place to fall freely. Because our evaluation requires tracking each individual structure, the drone attachment currently drops a single device. It can be extended to drop multiple devices simultaneously using a similar mechanism.

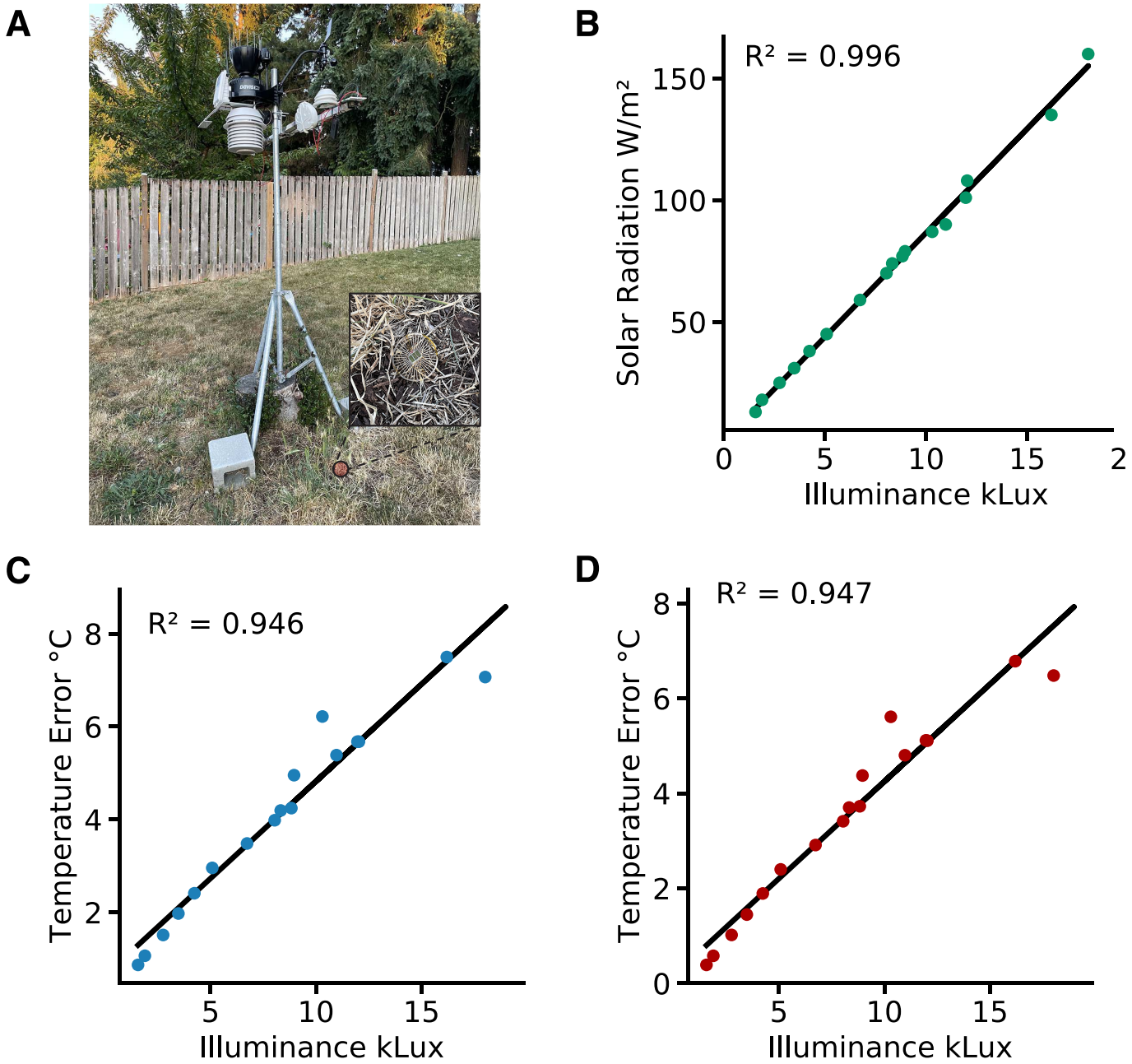

Extended Data Fig. 8 | Sensor calibration set-up using a weather station. **a**, Picture of weather station used for reference temperature, humidity, solar radiation and pressure measurements, and placement of the test wireless sensor node. **b**, Correlation of small onboard light sensor readings with reference solar radiation data. **c**, Correlation of small, onboard temperature sensor (HDC2010) readings with reference solar radiation data. **d**, Correlation of onboard temperature sensor temperature sensor (BME280) readings with reference solar radiation data.

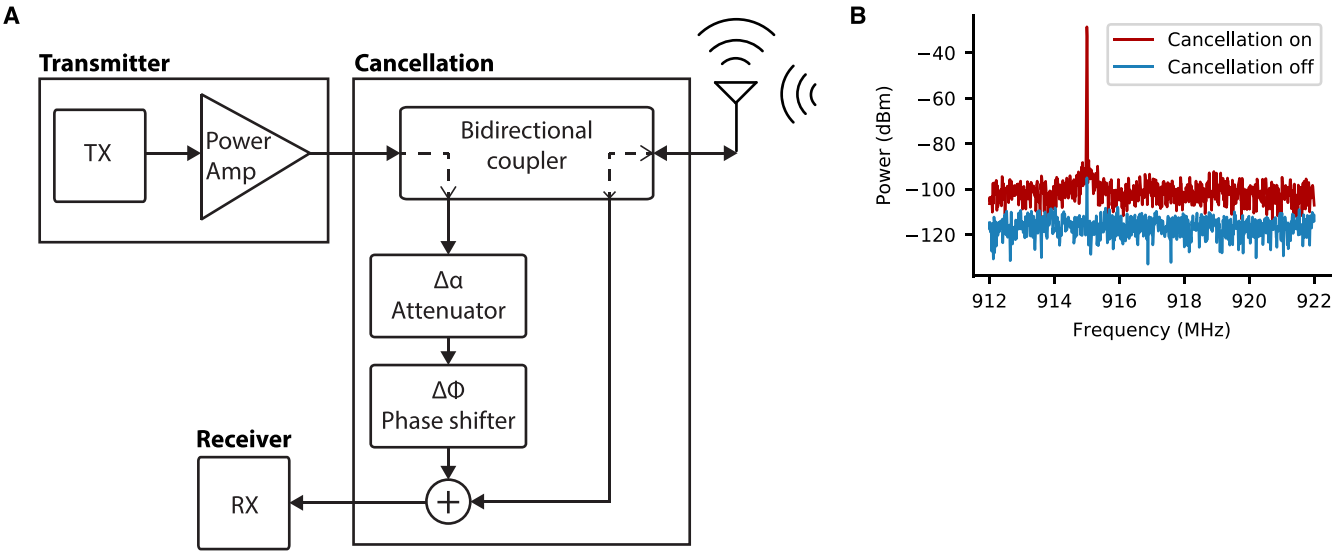

Extended Data Fig. 9 | Prototype full-duplex cancellation of our narrowband signals. a, Full-duplex cancellation block diagram. **b**, Results of applying full-duplex cancellation to reduce transmitter interference for backscatter.

Extended Data Table 1 | Sensor power measurements and part numbers

Sensor Type	Part numbers	Sensor mass (mg)	Memory (B)	Mode	On time (ms)	Peak current (mA)	Off current (µA)	Avg Current 1 Hz (µA)	1 Hz Min Lux	Avg Current 0.1 Hz (µA)	0.1 Hz Min Lux
Light	LV0104CS	1.4	540	Continuous	-	2.043	-	-	-	-	-
Temp	HDC2010	2.6	688	Continuous	-	2.345	-	-	-	-	-
Temp + RH	HDC2010	2.6	728	Cont.	-	2.326	-	-	-	-	-
Light + Temp + RH	LV0104CS, HDC2010	4	832	Cont.	-	2.06	-	-	-	-	-
Light + Temp + RH + Press	LV0104CS, BME280	12.4	974	Cont.	-	2.117	-	-	-	-	-
Magnetometer	MMC5633NJL	0.8	884	Cont.	-	5.396	-	-	-	-	-
Light	LV0104CS	1.4	608	Internal Timer	17.266	2.043	4.6	39.80	7200	8.12	4700
Temp	HDC2010	2.6	616	Internal Timer	4.806	2.345	4.665	15.91	4700	5.79	4700
Temp + RH	HDC2010	2.6	676	Internal Timer	5.354	2.326	4.665	17.09	4700	5.91	4700
Light + Temp + RH	LV0104CS, HDC2010	4	780	Internal Timer	21.27	2.06	4.72	48.44	9650	9.09	4700
Light + Temp + RH + Press	LV0104CS, BME280	12.4	922	Internal Timer	40.78	2.117	4.74	90.88	38000	13.35	4700
Magnetometer	MMC5633NJL	0.8	832	Internal Timer	5.076	5.396	5.82	33.18	6500	8.56	4700
Temp	HDC2010	2.6	674	External Timer	3.137	2.29	0.295	7.48	4700	1.01	1400
Temp + RH	HDC2010	2.6	734	External Timer	3.627	2.29	0.295	8.60	4700	1.13	1400
Light + Temp + RH	LV0104CS, HDC2010	4	838	External Timer	18.96	2.077	0.295	39.67	7200	4.23	1400